Global Frictional Equilibrium via Stochastic, Local Coulomb Frictional Slips

Shihuai Zhang[1] and Xiaodong Ma[2]

[1]Swiss Federal Institute of Technology in Zurich
[2]ETH Zürich

November 26, 2022

Abstract

Natural variability of fault friction and slip uncertainty exist in the Earth's crust. To what extent it influences crustal stress and its evolution is intriguing. We established a quasi-static, 2D model to simulate the stress evolution due to Coulomb frictional slips in the brittle crust. The model simply features randomly-oriented fractures with heterogeneous frictional coefficients. We emphasized the global stress response by summing the contribution of cascades of local frictional slip under specific boundary conditions. We illustrated that the decrease in stress difference manifests as a self-organized process that ultimately leads to frictional equilibrium. The model informs that the frictional equilibrium of a stochastic system can depart substantially from a deterministic estimation. Although the model quantitatively corroborates the notion of frictional equilibrium in places where fracture slip is the dominant mechanism for stress release, it reveals far more profound influence of system heterogeneity on the local and global stress evolution.

Global Frictional Equilibrium via Stochastic, Local Coulomb Frictional Slips

Shihuai Zhang and Xiaodong Ma*

Department of Earth Sciences, ETH Zürich, Zürich, Switzerland

*Corresponding author: Xiaodong Ma (xiaodongma.rocks@gmail.com)

Key Points:

- A simple quasi-static 2D model is introduced, quantifying and extending the classic notion of frictional equilibrium of the brittle crust
- We investigate the global scale stress evolution due to stochastic, local scale frictional slips in the crustal rock masses
- Frictional equilibrium of a stochastic system is greatly affected by its intrinsic friction heterogeneity

Abstract

Natural variability of fault friction and slip uncertainty exist in the Earth's crust. To what extent it influences crustal stress and its evolution is intriguing. We established a quasi-static, 2D model to simulate the stress evolution due to Coulomb frictional slips in the brittle crust. The model simply features randomly-oriented fractures with heterogeneous frictional coefficients. We emphasized the global stress response by summing the contribution of cascades of local frictional slip under specific boundary conditions. We illustrated that the decrease in stress difference manifests as a self-organized process that ultimately leads to frictional equilibrium. The model informs that the frictional equilibrium of a stochastic system can depart substantially from a deterministic estimation. Although the model quantitatively corroborates the notion of frictional equilibrium in places where fracture slip is the dominant mechanism for stress release, it reveals far more profound influence of system heterogeneity on the local and global stress evolution.

Plain Language Summary

Knowledge of crustal stress and its uncertainty is of fundamental importance to a wide range of problems. It is recognized that the intra-plate continental crust is generally in a state of frictional failure, the stress magnitudes of which usually cannot accumulate beyond the frictional strength. As a conventional practice, Coulomb theory is adopted together with laboratory-derived frictional coefficients for crustal stress estimations. Although it is able to attain a first-order agreement, such a practice has been primarily employed in a deterministic sense, which overlooks the fact that stress distribution is highly complex and spatially heterogeneous at different scales in the Earth's crust. In addition, how the upper crust keeps its stress magnitudes at its frictional strength is yet well understood. To this end, we proposed a simple quasi-static 2D model with distributed frictional coefficient as a proxy of the intrinsic system heterogeneity. By quantitatively investigating the global-scale stress evolution due to stochastic, local-scale frictional slips, this study shows that the magnitudes and uncertainties of both local- and global-scale stresses of the system can be greatly controlled by its friction heterogeneity. This model is believed to quantify and extend the classic notion of frictional equilibrium within the brittle crust.

1 Introduction

Fault slip is one of the dominant mechanisms for stress release in the Earth's upper crust. The stress of the fractured crust is often considered under 'frictional equilibrium', a dynamic status induced by ongoing tectonic/gravity loading and resulting fault slips (Zoback and Townend, 2001). Via the simple Coulomb frictional failure theory, the limiting state of stress can be conveniently expressed as:

$$\sigma_1/\sigma_3=\left(\sqrt{\mu^2+1}+\mu\right)^2 \tag{1}$$

where σ_1 and σ_3 are the effective major and minor principal stress, respectively, and μ is the frictional coefficient. Adopting laboratory-derived frictional coefficient values (μ = 0.6-1.0) (Byerlee, 1978), Eq.(1) has enabled the estimation of in situ stress and vice versa, the analysis of fault criticality (Brace and Kohlstedt, 1980; Townend and Zoback, 2000). However, to what spatial and temporal scale a deterministic use of Eq.(1) applies to is questionable, and has been often misused and mis-interpreted. Evidently, the value of μ varies spatially and temporally in the Earth's crust (Dieterich, 1979; Rivera and Kanamori, 2002), which underscores that such variability in a natural system must be considered.

To reflect such variability, recent attempts in stress estimation and/or fault slip analysis incorporated uncertainties in geomechanical parameters with a probabilistic approach (e.g., Walsh and Zoback, 2016; Hosseini et al., 2018; Luo and Ampuero, 2018), which offers more insights than a pure deterministic application of Eq.(1). However, one aspect still missing from existing stress models is how such system variability and heterogeneity influence the evolution of the in situ stress. How fault slip leads to frictional equilibrium, if possible, and whether it is attained is intriguing. The understanding of this evolution requires not only the influence of the far-field stress on the local fault slip, but also the feedback from the local slip to the global stress release. In this paper, we present a quasi-static, 2D model to simulate the stress evolution due to Coulomb frictional slip in the crustal rock masses. We explicitly consider frictional coefficient heterogeneity, as a proxy of the combined system uncertainties and variabilities, and emphasize the connection between the global and local stress response.

2 Methods

2.1 Model Configuration

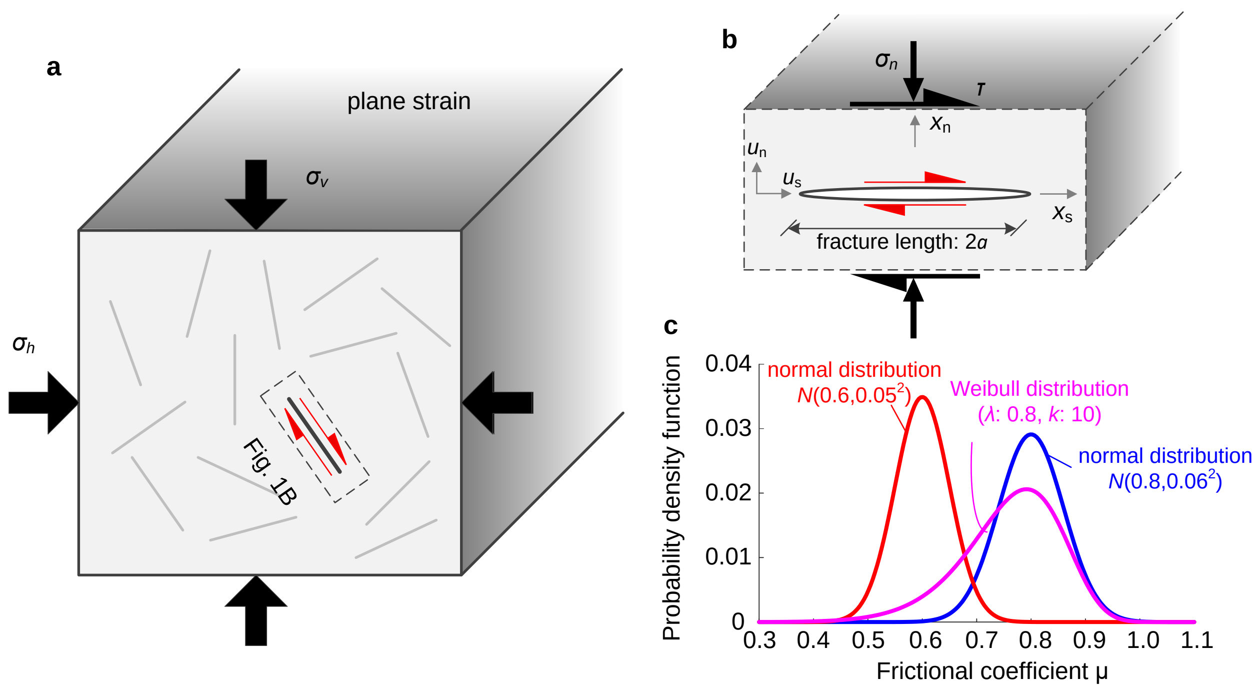

Figure 1. a Schematics of the plane strain model: randomly-distributed fractures in an elastic matrix subject to uniform stresses at the boundary. **b** Close-up of a fracture with its geometrical and mechanical features. **c** Distributions of frictional coefficient (μ) of fractures adopted to in the model.

The model we present is a fractured, elastic matrix configured under plane strain condition (Figure 1A). The embedded fractures are linear, planar, and cohesion-less. They are perpendicular to the plane section and through-going. The fractures are spatially characterized only by their orientations and their actual positions in the plane are irrelevant, see Text S1. This treatment follows Wiebols and Cook (1968) and other work on effective medium (Kachanov, 1992; Davy et al., 2018). Deemed essential to our model, the embedded fractures differ in their frictional coefficient μ, which can follow any arbitrary distribution, e.g., Figure 1C, as a proxy for the inherent heterogeneity in the system. The elastic matrix is simply characterized by its shear modulus G and Poisson's ratio v. As a quasi-static model for stress relaxation of much longer time scales, complex dynamic issues such as fracture initiation, propagation and termination are not addressed.

2.2 Local Slip – Shear Displacement

Given a remotely applied effective stress tensor σ at the model boundary, local shear and normal stresses (σ_n and τ) acting on individual fractures are mathematically expressed via the unit normal and shear vector, n and s, of each fracture. We are cognizant of stress perturbation near fractures, but considered it trivial in the context of upscaling (see Text S1). We simply adopt the classic Coulomb frictional failure criterion to determine whether slip occurs on a fracture. If $\tau > \mu \cdot \sigma_n$, the fracture is identified as critical and frictional slip occurs, otherwise the fracture stays perfectly bonded, behaving as part of the elastic matrix with no relative displacement occurring between opposite fracture sides. We assume that the shear stress on the fracture will drop to its frictional resistance after the slip, so that the shear stress difference $\Delta\tau = \tau - \mu \cdot \sigma_n$ drives the relative displacement across the fracture.

Based on elastic crack theory (Pollard and Segall, 1987), the normal and shear displacements (u_n and u_s) on opposite sides of a fracture associated with the slip can be analyzed conveniently in the local fracture coordinates (x_n, x_s) (Figure 1B). Specifically, they are:

$$u_\mathrm{n} = \Delta\tau \frac{1-2v}{2G} x_\mathrm{s} \tag{2a}$$

$$u_\mathrm{s}^{\pm} = \pm\Delta\tau \frac{1-v}{G} \sqrt{a^2 - x_\mathrm{s}^2} \tag{2b}$$

where $x_s \in [-a, a]$, a is the fracture half-length, and the superscript '±' of u_s refers to displacement along the upper and lower fracture side ($x_n = \pm 0$), respectively. The average relative shear displacement between opposite sides $\bar{\mathbf{d}}_\mathrm{s}$ is from integrating the relative shear displacement (u_s^{+}-u_s^{-}) across the fracture length:

$$\bar{\mathbf{d}}_\mathrm{s} = \left(\frac{1}{a}\int_0^a \Delta\tau \frac{2(1-v)}{G} \sqrt{a^2 - x_\mathrm{s}^2}\, \mathrm{d}x_\mathrm{s}\right) \mathbf{s} = \left(\Delta\tau \frac{a\pi(1-v)}{2G}\right) \mathbf{s} \tag{3a}$$

To reflect shear-induced dilatancy commonly observed in the brittle rock mass (Scholz, 1974; Fielding et al., 2009), we utilize dilatancy factor β to relate $\bar{\mathbf{d}}_\mathrm{s}$ to the average relative normal displacement $\bar{\mathbf{d}}_\mathrm{n}$:

$$\bar{\mathbf{d}}_\mathrm{n} = \beta |\bar{\mathbf{d}}_\mathrm{s}| \mathbf{n} = \beta \left(\Delta\tau \frac{a\pi(1-v)}{2G}\right) \mathbf{n} \tag{3b}$$

2.3 Upscaling Local Slips

We invoke Gaussian theorem (Hill, 1963; Kachanov, 1992) to relate the contribution of local displacement incurred by individual frictional slip to the global strain at the model boundary $\Delta\boldsymbol{\varepsilon}$:

$$\Delta\boldsymbol{\varepsilon}=\frac{a}{A}(\bar{\mathbf{d}}\otimes\mathbf{n}+\mathbf{n}\otimes\bar{\mathbf{d}}) \tag{4}$$

where A is the cross-section area of the model and $\bar{\mathbf{d}}=\bar{\mathbf{d}}_s+\bar{\mathbf{d}}_n$.

The total global strain at the model boundary comprises the strain of the intact elastic matrix $\boldsymbol{\varepsilon}^m$ and, if critical fractures exist, the summed strain $\Delta\boldsymbol{\varepsilon}$ induced by successive, individual slips of a cascade of critical fractures:

$$\boldsymbol{\varepsilon}_i=\boldsymbol{\varepsilon}^m+\sum_i\frac{a_i}{A}(\bar{\mathbf{d}}_i\otimes\mathbf{n}_i+\mathbf{n}_i\otimes\bar{\mathbf{d}}_i) \tag{5}$$

where subscript i denotes the ith fracture in a cascade of slips. The intact elastic matrix strain $\boldsymbol{\varepsilon}^m$ is simply regulated by Hooke's law under plane strain. Details on the slip cascades and upscaling are expanded in Text S2.

2.4 Slip Iterations, Time Steps

If stress and/or strain is mandated constant at the model boundary, the contribution of local fracture slips requires adjustment of stress/strain in the intact elastic matrix. This entails global stress adjustment at the model boundary and further modifies the criticality of individual fractures locally, necessitating a frequent re-evaluation of the fracture criticality. To this end, we impose an iterative process to accommodate the interplay between local fracture criticality, global stress and strain, and fractured matrix, tailored to the model experimentation below of specific boundary conditions (Text S2). We predicate the termination of the iteration when the shear stress difference $\Delta\tau$ of the most critical fracture is below 0.01 MPa. Constant slip rate depending on the global effective properties and local stress is assumed for each critical fracture within a time step, at the end of which the contribution of multiple slips is summed by the non-interaction approximation (Bristow, 1960) (expanded in Text S2).

3 Results

3.1 Model Experimentation in the Context of Normal Faulting Stress Regime

We start experimenting our model by simulating the simple scenario of stable intra-plate region with normal faulting stress environment ($\sigma_v = \sigma_1 > \sigma_h = \sigma_3$). The boundary condition is set with constant vertical stress and constant lateral strain. We assign the model with size A of 100×100 (in unit length), and 10,000 randomly-oriented fractures with equal length ($a_i \equiv a = 1$, unit length). The frictional coefficients of all fractures are normally distributed: the mean and the standard deviation of the distribution are 0.6 and 0.05, respectively, i.e., $N(0.6, 0.05^2)$ shown in Figure 1C. The dilatancy factor of fractures β is 0.05. The (intact) elastic matrix is assigned shear modulus G = 20 GPa and Poisson's ratio ν = 0.3.

We arbitrarily apply an effective stress tensor $\boldsymbol{\sigma}$ ($\sigma_{3,0}$ = 20 MPa, and $\sigma_{1,0}$ = 100 MPa) at the model boundary instantaneously at initial time t_0. It will become clear later in the text that the starting stress difference hardly matters to the final frictional equilibrium. Since no fracture slip occurs at t_0, $\varepsilon_{1,0}$ and $\varepsilon_{3,0}$ at the model boundary are only related to the elastic matrix response, i.e., $\varepsilon_{1,0} = \varepsilon_1^m$ and $\varepsilon_{3,0} = \varepsilon_3^m$. An initial evaluation of fracture criticality allows the iterative slip process to begin. Mohr diagrams are used to illustrate the first two time steps as an example (Figure 2). The slip of critical fractures reduces the shear stresses on themselves to their frictional resistance, revealing local stress heterogeneities in the system. Upon the end of a time step, i.e., a cascade of slips, boundary stress σ_3 is increased to maintain constant lateral strain and fracture criticality evaluation re-iterates. With the starting stress difference substantially above the possible equilibrium state, the stress evolution undergoes multiple time steps (1, 2, …, j, …) before it terminates (see details in Text S2). As the vertical stress σ_1 is held constant, the horizontal stress $\sigma_{3,j}$ increases, or, the stress difference ($\sigma_{1,j}$ - $\sigma_{3,j}$) relaxes monotonically. The stress evolution at the model boundary manifests itself as a series of contracting Mohr diagrams (Figure 3A). The number of fracture slips and the amount of stress relaxation of each time step diminishes significantly as the iteration continues. Numerous fracture slips induce the accumulation of vertical strain and the reduction of system stiffness, as illustrated in Figure 3B. Such response is characteristic of the absence of tectonic loading.

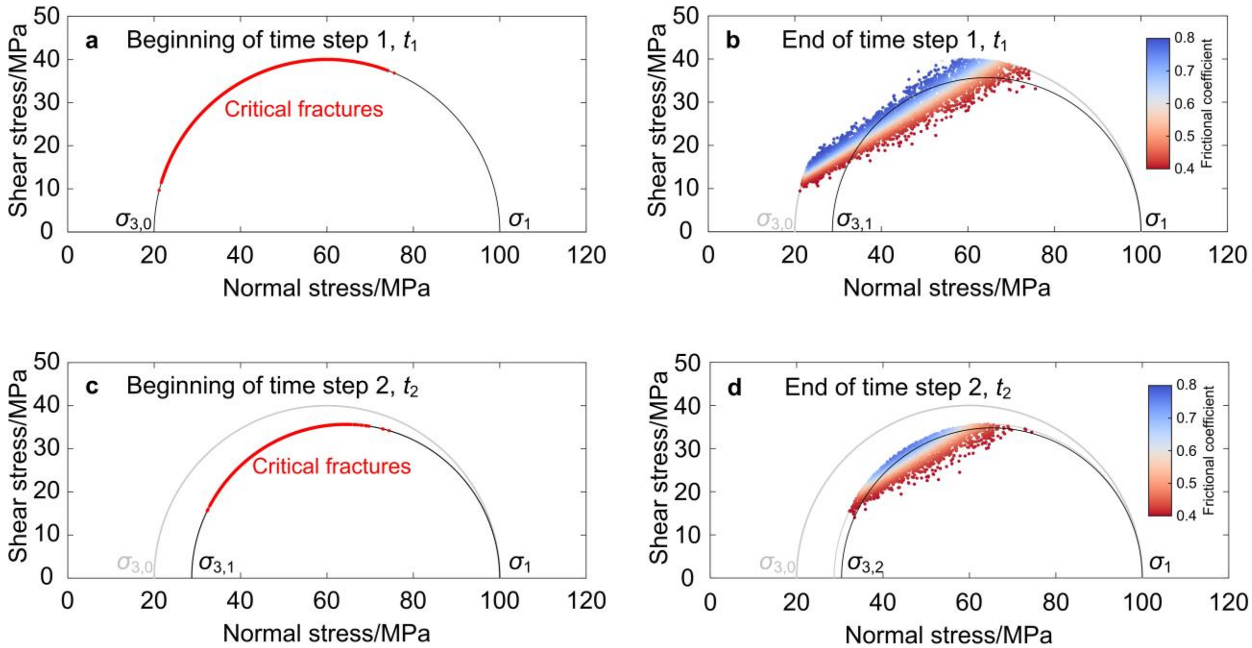

Figure 2. Mohr diagrams illustrating the first two iterations of stress evolution from an arbitrary, initial stress condition within the normal faulting stress regime. The fractures in the system follow a normally distributed frictional coefficient $N(0.6, 0.05^2)$. **a**, **c**: Beginning each time step, critical fractures (red) are identified. **b**, **d**: After a cascade of local fracture slips within the time step, shear stress of each critical fracture drops to its frictional resistance, which results in the global stress update, i.e., σ_3 increase.

The model's final stress state, or frictional equilibrium, is attained when iterations terminate. The most critical fracture in the system can be located. Retrospectively, the stress state and frictional resistance of the most critical fracture through the iterations can be traced, as illustrated in Figure 3A. Evidently, the fracture keeps slipping as long as its shear stress is larger than but converges towards its frictional resistance. The linear trace of the fracture frictional resistance can be interpreted as the equivalent frictional strength of the system, that is, μ = 0.43.

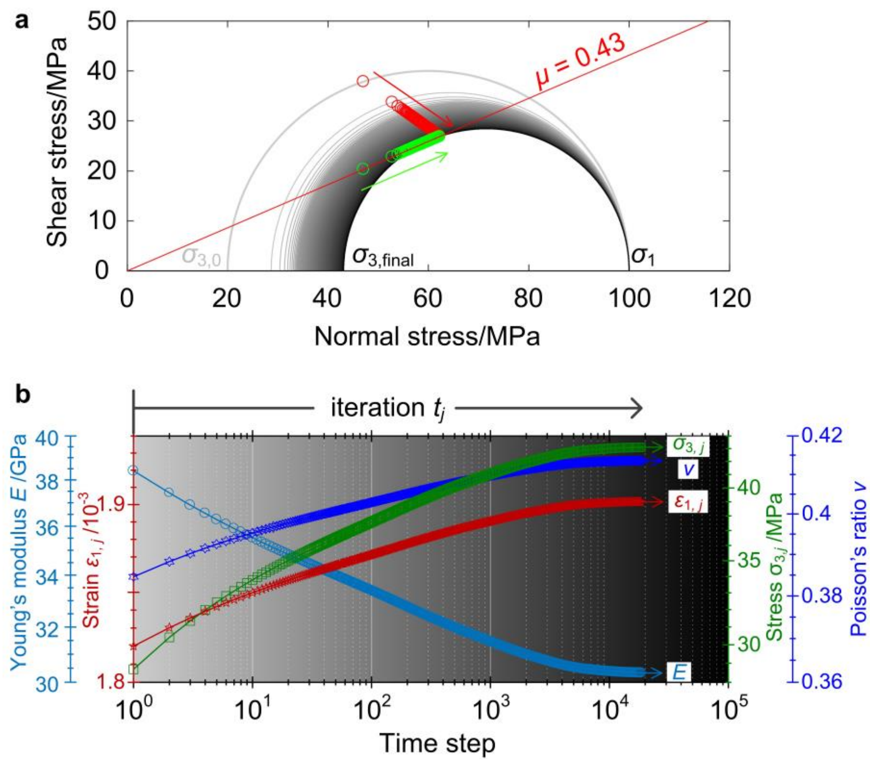

Figure 3. Overview of the temporal evolution of the model specified in Figure 2. **a** The stress relaxation due to cascades of fracture slips is illustrated by contracting Mohr diagrams. The final stress state rests on the frictional envelop (μ = 0.43), which is in fact controlled by the most critical fracture in the system. Red and green circles represent the resolved stress state and frictional resistance on the most critical fracture at each time step. **b** Evolving stress (σ), strain (ε), Young's modulus (E), and Poisson's ratio (ν) through iterations. Note the rate of change in these parameters gradually diminishes towards the final stress state. Gray scale color scheme in **a** and **b** corresponds to iterations (logarithmic).

3.2 More on Heterogeneous Frictional Coefficient

Comparing this stochastic treatment with the deterministic case in which the frictional coefficients of all fractures are homogeneous (μ = 0.6, see Text S3), the final σ_3 upon equilibrium of the former is smaller than that of the latter, intuitively indicated in Figure 4A. Apparently, the maximum stress difference that can be sustained by the stochastic system does not depend on the mean or the upper bound of the frictional coefficient distribution. This is further demonstrated by two additional distributions, i.e., normal distribution $N(0.8, 0.06^2)$ and Weibull distribution with scale parameter λ = 0.8 and shape parameter k = 10, as illustrated in Figure 4B and 4C, respectively.

Further reviewing the stress evolution of each distribution, we identified that the frictional coefficient of the most critical fracture does not necessarily correspond to the lowest value, as one would assume, but it is located close to the lower bound of the distribution. Monte Carlo simulations shows such an observation is of high probability (Text S4). This suggests that the most critical fracture is determined jointly by its frictional coefficient and orientation with respect to the global stress. That said, the equivalent frictional strength of the fractured matrix is dependent on the combination of frictional coefficient distribution and orientations of all fractures. As indicated by Figure 4, the uncertainty of the equivalent frictional strength becomes more evident when the μ distribution departs further from uniformity, which also implies the degree of heterogeneity of global stress in such a stochastic system. Therefore, when inferring the state of stress in situ assuming frictional equilibrium, the practical value of frictional coefficient to be adopted is of utter importance.

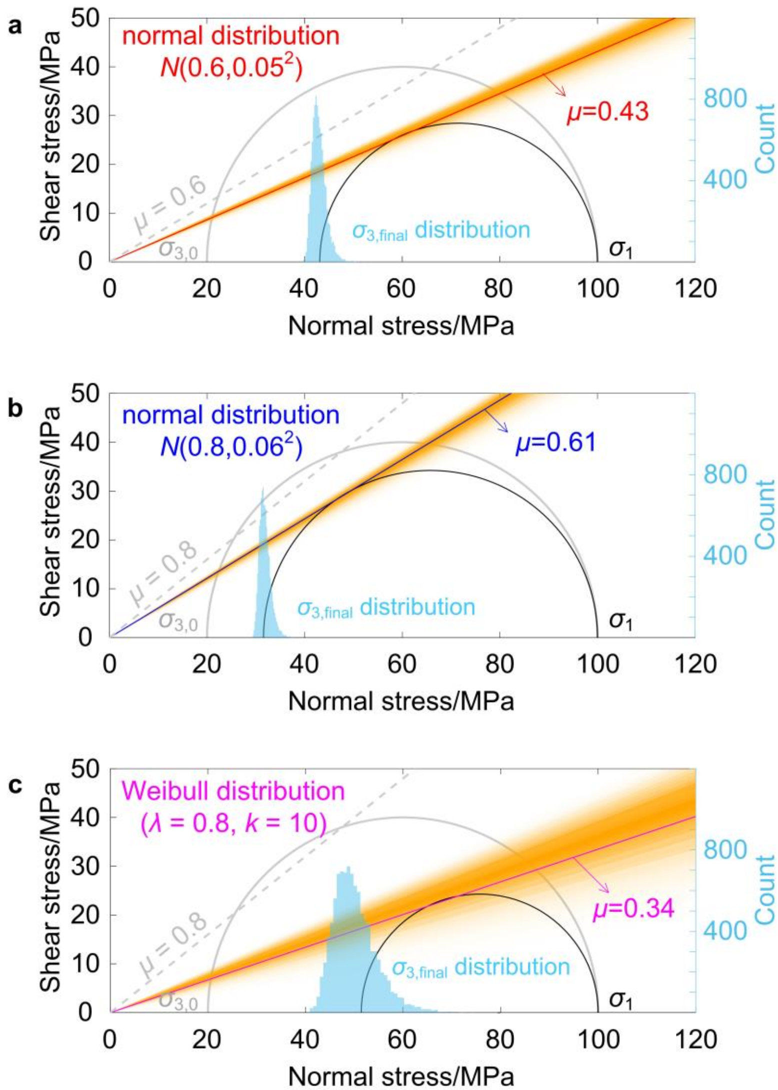

Figure 4. Initial (gray) and final (black) stress state for the same model configuration but different frictional coefficient distributions. The most probable final stress state, bounded by the corresponding equivalent frictional coefficient of the system, is associated with uncertainties (fuzzy lines or the distribution of σ_3, see Figure S6 for more details).

4 Conclusions

The model extends the notion of frictional equilibrium. For the deterministic interpretation in which the frictional coefficient is homogeneous, the frictional equilibrium refers to a state prescribed by Eq. (1). In a heterogeneous system, the frictional equilibrium can be understood as a dynamic process as illustrated in the model experimentation, spanning from the very first frictional slip to the final one possibly allowed by the prevailing in situ stress difference. The use of Eq. (1) in this instance therefore incurs great uncertainty. Informed by the numerous time steps leading to the final frictional equilibrium, the most critical fracture or fault stays critical while the rest of the crust experiences practically few slips, i.e., little global stress reduction. The apparent discrepancy between the local and global response reflects the stress heterogeneity within the system, which is jointly regulated by the variability of frictional coefficient and orientation of the fractures. To this end, the controversy over whether the upper crust is critically stressed is plausibly resolved. Again, we emphasize that the dominant mechanism of stress release in this context is frictional slip. Other mechanisms that may further lower the stress difference below frictional equilibrium in certain lithologies, such as viscoplastic deformation in shales (Sone and Zoback, 2014; Ma and Zoback, 2017), pressure solution in carbonates (Gunzburger and Cornet 2007; Gratier et al., 2013; Brantut et al., 2014), are not addressed here.

The evolution of stress reduction raises questions about the stage at which the current state of stress is with respect to the equilibrium. This is informative to stress estimation and fault slip tendency analysis. Note that in our model, the evolution iterates through ‘pseudo’ time steps and is not calibrated against real time. This is a compromise for computational feasibility and efficiency, so the interpretation in a temporal sense should be executed with caution. Nonetheless, the time-dependent stress reduction and matrix response appears to be reasonable and is deemed of first-order importance. Because of the difficulty to impose real time in the model, we were unable to experiment boundary conditions with prescribed strain or stress rate, which is more realistic in tectonically active regions. It is worth noting that no fracture interaction, extension and matrix damage was allowed in the model. If that was the case, the expected stress reduction will be more significant due to increased number and length of fractures and lowered equivalent matrix stiffness. The equivalent frictional strength of the crust will be even lower, in other words, the difference between the reality and the deterministic model will be more substantial.

Acknowledgments

This work is supported by Swiss National Science Foundation (grant No. 182150) and benefited from discussions with Norman Sleep and Hiroki Sone. This is a theoretical study and contains no collected data. The scripts used to produce the results can be requested from the authors.

References

Brace, W. F., & Kohlstedt, D. L. (1980). Limits on lithospheric stress imposed by laboratory experiments. *Journal of Geophysical Research: Solid Earth*, *85*(B11), 6248-6252. doi: 10.1029/JB085iB11p06248.

Brantut, N., Heap, M. J., Baud, P., & Meredith, P. G. (2014). Mechanisms of time-dependent deformation in porous limestone. *Journal of Geophysical Research: Solid Earth*, 119(7), 5444-5463. doi: 10.1002/2014JB011186.

Bristow, J. R. (1960). Microcracks, and the static and dynamic elastic constants of annealed and heavily cold-worked metals. British Journal of Applied Physics, 11(2), 81.

Byerlee, J. (1978). Friction of rocks. In Rock friction and earthquake prediction (pp. 615-626). Birkhäuser, Basel. doi: 10.1007/978-3-0348-7182-2_4.

Davy, P., Darcel, C., Le Goc, R., & Mas Ivars, D. (2018). Elastic properties of fractured rock masses with frictional properties and power law fracture size distributions. *Journal of Geophysical Research: Solid Earth*, 123(8), 6521-6539. doi: 10.1029/2017JB015329.

Dieterich, J. H. (1979). Modeling of rock friction: 1. Experimental results and constitutive equations. *Journal of Geophysical Research: Solid Earth*, 84(B5), 2161-2168. doi: 10.1029/JB084iB05p02161.

Fielding, E. J., Lundgren, P. R., Bürgmann, R., & Funning, G. J. (2009). Shallow fault-zone dilatancy recovery after the 2003 Bam earthquake in Iran. *Nature*, 458(7234), 64-68. doi: 10.1038/nature07817.

Gratier, J. P., Dysthe, D. K., & Renard, F. (2013). The role of pressure solution creep in the ductility of the Earth's upper crust. In *Advances in Geophysics* (Vol. 54, pp. 47-179). Elsevier. doi: 10.1016/B978-0-12-380940-7.00002-0.

Grechka, V., & Kachanov, M. (2006). Effective elasticity of fractured rocks: A snapshot of the work in progress. *Geophysics*, 71(6), W45-W58. doi: 10.1190/1.2360212.

Gunzburger, Y., & Cornet, F. H. (2007). Rheological characterization of a sedimentary formation from a stress profile inversion. *Geophysical Journal International*, 168(1), 402-418. doi: 10.1111/j.1365-246X.2006.03140.x.

Healy, D. (2008). Damage patterns, stress rotations and pore fluid pressures in strike-slip fault zones. *Journal of Geophysical Research: Solid Earth*, 113(B12). doi: 10.1029/2008JB005655.

Hill, R. (1963). Elastic properties of reinforced solids: some theoretical principles. *Journal of the Mechanics and Physics of Solids*, 11(5), 357-372. doi: 10.1016/0022-5096(63)90036-X.

Hosseini, S. M., Goebel, T. H. W., Jha, B., & Aminzadeh, F. (2018). A Probabilistic Approach to Injection-Induced Seismicity Assessment in the Presence and Absence of Flow Boundaries. *Geophysical Research Letters*, 45(16), 8182-8189. doi: 10.1029/2018GL077552.

Kachanov, M. (1992). Effective elastic properties of cracked solids: critical review of some basic concepts. *Applied Mechanics Reviews*, 45(8), 304-335. doi: 10.1115/1.3119761.

Katz, O., & Reches, Z. E. (2004). Microfracturing, damage, and failure of brittle granites. *Journal of Geophysical Research: Solid Earth*, 109(B1). doi: 10.1029/2002JB001961.

Luo, Y., & Ampuero, J. P. (2018). Stability of faults with heterogeneous friction properties and effective normal stress. *Tectonophysics*, 733, 257-272. doi: 10.1016/j.tecto.2017.11.006.

Ma, X., & Zoback, M. D. (2017). Lithology-controlled stress variations and pad-scale faults: A case study of hydraulic fracturing in the Woodford Shale, OklahomaWoodford Shale case study. *Geophysics*, 82(6), ID35-ID44. doi: 10.1190/geo2017-0044.1.

Napier, J. A. L., & Malan, D. F. (1997). A viscoplastic discontinuum model of time-dependent fracture and seismicity effects in brittle rock. *International Journal of Rock Mechanics and Mining Sciences*, 34(7), 1075-1089. doi: 10.1016/S1365-1609(97)90201-X.

Perzyna, P. (1966). Fundamental problems in viscoplasticity. In *Advances in applied mechanics* (Vol. 9, pp. 243-377). Elsevier.

Pollard, D. D., & Segall, P. (1987). Theoretical displacements and stresses near fractures in rock: with applications to faults, joints, veins, dikes, and solution surfaces. In Fracture mechanics of rock (pp. 277-347).

Rivera, L., & Kanamori, H. (2002). Spatial heterogeneity of tectonic stress and friction in the crust. *Geophysical research letters*, 29(6), 12-1. doi: 10.1029/2001GL013803.

Ruina, A. L. (1980). Friction laws and instabilities: a quasi-static analysis of some dry friction behaviour. *Ph. D. thesis, Division of Engineering, Brown University*.

Scholz, C. H. (1974). Post-earthquake dilatancy recovery. *Geology*, 2(11), 551-554. doi: 10.1130/0091-7613(1974)2<551:PDR>2.0.CO;2.

Sleep, N. H. (2006). Real contacts and evolution laws for rate and state friction. *Geochemistry, Geophysics, Geosystems*, 7(8). doi: 10.1029/2005GC001187.

Sone, H., & Zoback, M. D. (2014). Time-dependent deformation of shale gas reservoir rocks and its long-term effect on the in situ state of stress. *International Journal of Rock Mechanics and Mining Sciences*, 69, 120-132. doi: 10.1016/j.ijrmms.2014.04.002.

Townend, J., & Zoback, M. D. (2000). How faulting keeps the crust strong. *Geology*, 28(5), 399-402. doi: 10.1130/0091-7613(2000)28<399:HFKTCS>2.0.CO;2.

Walsh III, F. R., & Zoback, M. D. (2016). Probabilistic assessment of potential fault slip related to injection-induced earthquakes: Application to north-central Oklahoma, USA. *Geology*, 44(12), 991-994. doi: 10.1130/G38275.1.

Wiebols, G. A., & Cook, N. G. W. (1968, November). An energy criterion for the strength of rock in polyaxial compression. In *International Journal of Rock Mechanics and Mining Sciences & Geomechanics Abstracts* (Vol. 5, No. 6, pp. 529-549). Pergamon. doi: 10.1016/0148-9062(68)90040-5.

Zoback, M. D., & Townend, J. (2001). Implications of hydrostatic pore pressures and high crustal strength for the deformation of intraplate lithosphere. *Tectonophysics*, 336(1-4), 19-30. doi: 10.1016/S0040-1951(01)00091-9.

Geophysical Research Letters

Supporting Information for

Global Frictional Equilibrium via Stochastic, Local Coulomb Frictional Slips

Shihuai Zhang and Xiaodong Ma

Department of Earth Sciences, ETH Zürich, Zürich, Switzerland

Contents of this file

Introduction

In this supplementary material, we expand on the methods and results to complement the main manuscript. In Text S1, we describe how to calculate the shear and normal stresses on fractures and discuss the major assumptions adopted in this model. In Text S2, we elaborate on the slip cascades and their contribution to the global stress/strain fields, followed by an example displaying the iterative process in the context of normal faulting stress regime. We then show the stress evolution in the deterministic case where all fractures have the same frictional coefficient in Text S3. Monte Carlo simulation and system uncertainty analysis are detailed in Text S4. For each frictional coefficient distribution, finally in Text S5, simulation results in the context of reverse faulting regime are provided for comparison.

Text S1. Individual Fractures, Local Frictional Slips

Given a stress tensor $\boldsymbol{\sigma}$ applied remotely at the model boundary, the stress acting on any arbitrarily-oriented fictitious fracture plane can be resolved by transformation. The normal and shear stress component (σ_{n} and τ) on a fracture plane can be resolved with the plane's unit normal and shear vector (**n** and **s**) (Davy et al., 2018):

$$\sigma_{\mathrm{n}} = \mathbf{n} \cdot \boldsymbol{\sigma} \cdot \mathbf{n} \tag{S1}$$

$$\tau = \mathbf{n}^{\mathrm{T}} \cdot \boldsymbol{\sigma} \cdot \mathbf{s} \tag{S2}$$

where

$$\mathbf{s} = \frac{\mathbf{s}_g}{|\mathbf{s}_g|},\ \mathbf{s}_g^{\mathrm{T}} = \mathbf{n}^{\mathrm{T}} \cdot \boldsymbol{\sigma} \cdot \left(\mathbf{I} - \mathbf{n} \otimes \mathbf{n}^{\mathrm{T}}\right) \tag{S3}$$

where **I** is the identity matrix. Intuitively, the Mohr diagram graphically represents the initial stresses acting on fractures, as shown in Figure 2. In our model, the fracture orientation is differentiated by the angle (θ) between the normal to the fracture and the positive hortizontal axis of the model's global coordinates (Figure S1). Note that, for convenience, we only consider the normal vector of the upward facing fracture side, i.e., $\theta \in [0,180°]$.

Local stress fluctuations induced by nearby fracture interactions can be profound in a rock mass. However, such effect is not considered in this model. By assuming a uniform spatial distribution of fracture centers, i.e., no fracture clusters exist, strong fracture interactions can be plausibly circumvented. The mutually opposite effects of stress shielding and amplification near fractures tend to balance out globally, given the statistical significance of assuming uniform fracture orientations (Kachanov, 1992). Such assumptions have been validated by comparing the theoretically predicted results either with numerical simulations (Grechka and Kachanov, 2006) or with laboratory observations (Katz and Reches, 2004), and have been widely adopted to quantify the effective properties of fractured rock masses (e.g., Healy, 2008; Davy et al., 2018).

Text S2. More on Upscaling Slip Cascades and Iterative Time Steps

Slip rate within a time step

The slip rate is considered variable, which is dependent on the past slip history and stress state (Dieterich, 1979; Ruina, 1980, Sleep, 2006). To reflect this in the iterations, a simple linear relationship between fracture slip rate and shear stress difference $\Delta\tau$ is proposed:

$$\frac{d\bar{\mathbf{d}}_{\mathrm{s}}}{dt} = (\eta\Delta\tau)\mathbf{s} \tag{S4a}$$

$$\frac{d\bar{\mathbf{d}}_{\mathrm{n}}}{dt} = (\beta\cdot\eta\Delta\tau)\mathbf{n} \tag{S4b}$$

where η is defined as slip rate parameter with the dimension of length/(stress·time), similar to the fluidity parameter of classical viscoplasticity theory (Perzyna, 1966; Napier and Malan, 1997).

In discrete form, the relative shear and normal displacement increments can be further expressed as:

$$\Delta\left|\bar{\mathbf{d}}_{\mathrm{s}}\right|_{j} = \left(\eta_j\Delta\tau_{j-1}\right)\cdot\Delta t \tag{S5a}$$

$$\Delta\left|\bar{\mathbf{d}}_{\mathrm{n}}\right|_{j} = \left(\beta\cdot\eta_j\Delta\tau_{j-1}\right)\cdot\Delta t \tag{S5b}$$

where

$$\Delta t = t_j - t_{j-1}, j = 1,2,3,\ldots \tag{S5c}$$

which implies that the updated results at the end of the previous time step (j-1) serve as the new input and are kept constant over the current time step (j). If frictional slip is assumed to occur completely and reach the final steady state at the end of each time step, the slip rate parameter η_j can be simply specified according to Eq. (3) as:

$$\eta_j = \frac{a\pi\left(1-v_{j-1}\right)}{2G_{j-1}} \tag{S6}$$

which means that η at the jth time step is the function of the current effective elastic properties, qualitatively incorporating the effect of slip history to some extent although the frictional coefficient is kept constant.

Non-Interaction Approximation (NIA)

In addition, the Non-Interaction Approximation (NIA) is adopted at the end of the jth time step to calculate the eventual global strain by summing the contribution of all fractures slips. NIA originally assumes that any new fracture is surrounded by an undamaged elastic medium. Here we hypothesize that, within the jth time step, all critical fractures slip in an unchanged, homogeneous effective medium, which are the average properties updated at the end of the (j-1)th time step.

An example of iterative process

At the beginning of each time step, the elastic matrix strain $\boldsymbol{\varepsilon}^{\mathrm{m}}$ is first estimated according to Hooke's law under the plane strain condition:

$$\boldsymbol{\varepsilon}^m = \begin{bmatrix}\varepsilon_1^m\\ \varepsilon_3^m\end{bmatrix} = \frac{1-v}{2G}\begin{bmatrix}1 & -v/(1-v)\\ -v/(1-v) & 1\end{bmatrix}\begin{bmatrix}\sigma_1\\ \sigma_3\end{bmatrix} \tag{S7}$$

The relative displacement increments of each critical fracture within the time step are obtained based on Eq. (S5), Eq. (S6), and NIA, which are related to the global strain increments by Eq. (4) and further summed up to quantify the eventual additional strain tensor $\Delta\boldsymbol{\varepsilon}_{\mathrm{total},\,j}$:

$$\Delta\boldsymbol{\varepsilon}_{\mathrm{total}} = \begin{bmatrix}\Delta\varepsilon_1\\ \Delta\varepsilon_3\end{bmatrix} \tag{S8}$$

Taking compression as positive, $\Delta\varepsilon_3$ is always negative due to the fracture-induced dilation in the direction of the minor principal stress (σ_3). In the context of normal faulting stress regime, in which horizontal strain $\varepsilon_h = \varepsilon_3$ at boundary is maintained constant, the hortizontal strain of the elastic matrix ε_3^m needs to increase to accommodate $\Delta\varepsilon_3$, which is self-regulated by σ_3 increase.

Treating the model as an effective medium and invoking Hooke's law, we have the strain response at the *j*th time step as:

$$\varepsilon_{3,j} = \frac{1-v_{j-1}}{2G_{j-1}}\left(\frac{-v_{j-1}}{1-v_{j-1}}\sigma_{1,j-1} + \left(\sigma_{3,j-1} - \Delta\sigma_{3,j}\right)\right) + \Delta\varepsilon_{3,j} = \varepsilon_{3,0} \tag{S9}$$

which further gives:

$$\Delta\sigma_{3,j} = \frac{2G_{j-1}}{1-v_{j-1}}\Delta\varepsilon_{3,j} \tag{S10}$$

and

$$\sigma_{3,j} = \sigma_{3,j-1} - \Delta\sigma_{3,j} = \sigma_{3,j-1} - \frac{2G_{j-1}}{1-v_{j-1}}\Delta\varepsilon_{3,j} \tag{S11}$$

It implies a monotonic increase of σ_3 after each time step given a dilational $\Delta\varepsilon_{3,j}$. Accordingly, the updated strain $\varepsilon_{1,j}$ can be calculated by:

$$\varepsilon_{1,j} = \varepsilon_{1,j-1} + \frac{v_{j-1}}{2G_{j-1}}\Delta\sigma_{3,j} + \Delta\varepsilon_{1,j} \tag{S12}$$

where the second right-hand term reflects the Poisson effect induced by the increase of σ_3 and the third term is the slip-contributed strain increase. It should be noted that, the vertical stress is always constant in the normal faulting regime, i.e., $\sigma_v = \sigma_{1,0} = \sigma_{1,1} = \cdots = \sigma_{11,j-1} = \sigma_{11,j}$. With the updated global stress and strain at the boundary, effective elastic parameters (G_{j-1} and v_{j-1}) are updated by solving equations in Eq. (S7) at the end of the *j*th time step, acting as the input of the (*j*+1)th time step.

In addition to Figure 3**b**, more detailed information about the iterative process for frictional coefficient distribution $N(0.6, 0.05^2)$ can be found in Figure S2. The temporal variations of the slip rate parameter, slip rate, and shear stress difference of the most critical fracture show that the drastic rate of change in the first 1,000 time steps. The number of critical fractures within each time step further shows that it decreases rapidly from initially about 4,300 to 3 at around the 900$^{\text{th}}$ time step, explaining the slow growth of mechanical parameters during the subsequent tens of thousands of time steps as shown in Figure 3**b**. We also present the stochastic cases with frictional coefficient distribution (1) normal distribution $N(0.8, 0.06^2)$ and (2) Weibull distribution (scale parameter λ = 0.8 and shape parameter k = 10) in Figure S3 and Figure S4, respectively, where the first two iterations and the complete stress evolution process are included. As with the case specified in Figure 2, it confirms that the stochastic treatment of frictional coefficient is able to enable the model with local stress heterogeneity.

Text S3. Stress evolution for the deterministic case

For comparison, uniform frictional coefficient is assigned to all fractures while the model configuration remains the same. In Figure S5**a-d**, the first two iterations suggest a deterministic stress evolution process for the deterministic case. In other words, the equivalent frictional strength of the model is doubtlessly 0.6. At the beginning of each time step, all fractures lying above the frictional failure envelope are critical, which is not the case in the stochastic systems as shown in Figure 2 (or Figure S3 and Figure S4). In addition, shear stresses of all critical fractures will drop onto the single frictional failure line, i.e., frictional resistance. Due to the absence of heterogeneity, the deterministic system takes only 98 time steps to reach the final frictional equilibrium, as shown in Figure S5**e**. This gives a quantitative interpretation of the classic notion of frictional equilibrium and also confirms that the very control of the most critical fracture on the global stress state.

Text S4. Monte Carlo simulation, system uncertain analysis

Whether a fracture is critical or not depends on its frictional coefficient and orientation with respect to the global stress field. As both parameters are randomly generated in each experimentation, it is imperative to examine the uncertainty associated with this stochastic model. To this end, we run 10,000 Monte Carlo simulations to repeat the iterative process. Primarily, we quantify the probability of the frictional coefficient and orientation of the most critical fracture, to see if it stays invariant to support our conclusions.

For each simulation, the frictional coefficient and orientation of the fractures are randomly generated according to the respective distribution. We apply the same initial stress difference ($\sigma_h = \sigma_{1,0} = 100$ MPa > $\sigma_v = \sigma_{3,0} = 20$ MPa) in the normal faulting scenario (shown in Figure 4). It is then able to identify the most critical fracture by determining the largest shear stress difference $\Delta\tau$. Figure S6 shows the distributions of the frictional coefficient and orientation of the most critical fracture in different cases. In Figure S6**a-c**, we confirm that the frictional coefficient of the most critical fracture falls at the lower end of its distribution. With regard to the orientation, the most critical fracture orients approximately at an angle of 60° or 120° to the global horizontal axis, as shown in Figure S6**d-f**. In addition, the uncertainty of both parameters increases as the system becomes more heterogeneous. It should be noted that the final Mohr circle is not necessary tangent to the frictional failure envelope in the stochastic case. As an end-member, the frictional coefficient and orientation of the most critical fracture in the deterministic case are also deterministic (Figure S5). Since frictional coefficient distribution is used as a proxy of system heterogeneity, it is concluded that the global response also has remarkable uncertainty which depends largely on the intrinsic heterogeneity. In the context of normal faulting stress regime, such uncertainty can be represented by distributed frictional failure envelope, or more quantitatively, by the probability density function of effective minor principal stress σ_3 determined at the end of each simulation, as shown in Figure 4.

Text S5. Stress evolution in the context of reverse faulting stress regime

For each distribution, we also experimented the model in the context of reverse faulting regime. To facilitate comparison, we set the same starting stress difference ($\sigma_h = \sigma_{1,0} = 100$ MPa > $\sigma_v = \sigma_{3,0} = 20$ MPa). We maintain the boundary condition of constant vertical stress and constant lateral strain. Based on the expressions in the normal faulting case, we can obtain similar derivations simply by switching the numeric subscripts '1' and '3' of each term in Eq. (S11), which gives:

$$\sigma_{1,j} = \sigma_{1,j-1} - \Delta\sigma_{1,j} = \sigma_{1,j-1} - \frac{2G_{j-1}}{1-v_{j-1}}\Delta\varepsilon_{1,j} \tag{S13}$$

Note that, $\Delta\varepsilon_{1,j}$ is positive due to compression in this scenario. Therefore, σ_1 will decrease and the updated strain $\varepsilon_{3,j}$ can be calculated by:

$$\varepsilon_{3,j} = \varepsilon_{3,j-1} + \frac{v_{j-1}}{2G_{j-1}}\Delta\sigma_{1,j} + \Delta\varepsilon_{3,j} \tag{S14}$$

Figure S7-S9 show the first two iterations and the whole stress evolution process for frictional coefficient distribution (1) normal distribution $N(0.8, 0.06^2)$, (2) normal distribution $N(0.6, 0.05^2)$, and (3) Weibull distribution ($\lambda = 0.8$, $k = 10$), respectively. As expected, lateral stress $\sigma_{1,j}$ decreases to allow for the reduction of stress difference due to frictional slip. The final stress difference is smaller than that of the normal faulting scenario, for any distribution, and it takes much more time steps reach the final frictional equilibrium. We further note that, for each distribution, the frictional equilibrium in both stress regimes is bounded by the same equivalent frictional strength. This reveals that the equivalent frictional strength of the model is independent of the applied boundary conditions, but characteristic of the stochastic nature of the fractures therein. In addition, the deterministic case in reverse faulting regime is shown in Figure S10. As with the stochastic cases, it takes much more time steps to reach the final frictional equilibrium than the normal faulting scenario.

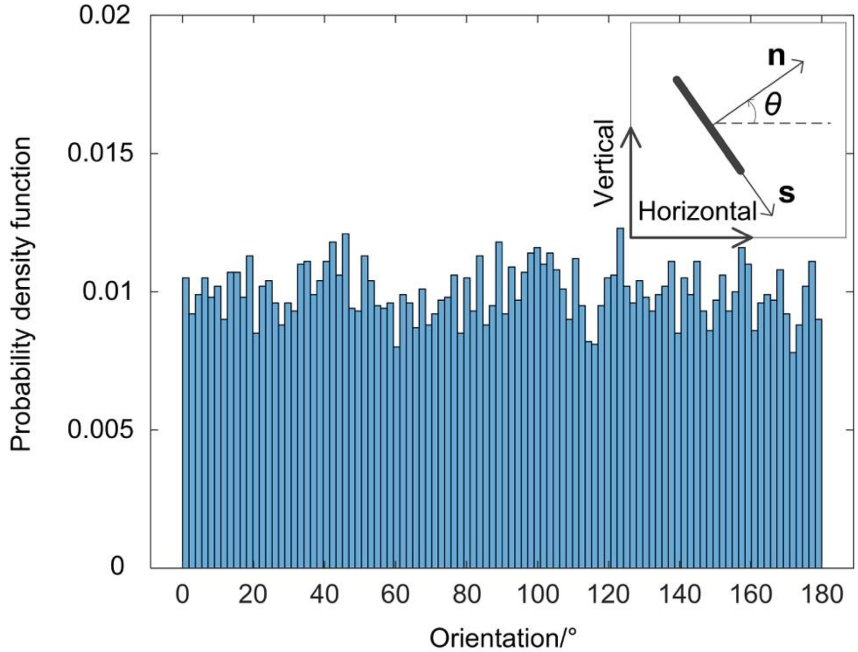

Figure S1. Uniform distribution of fracture orientation, which is defined schematically in the inset.

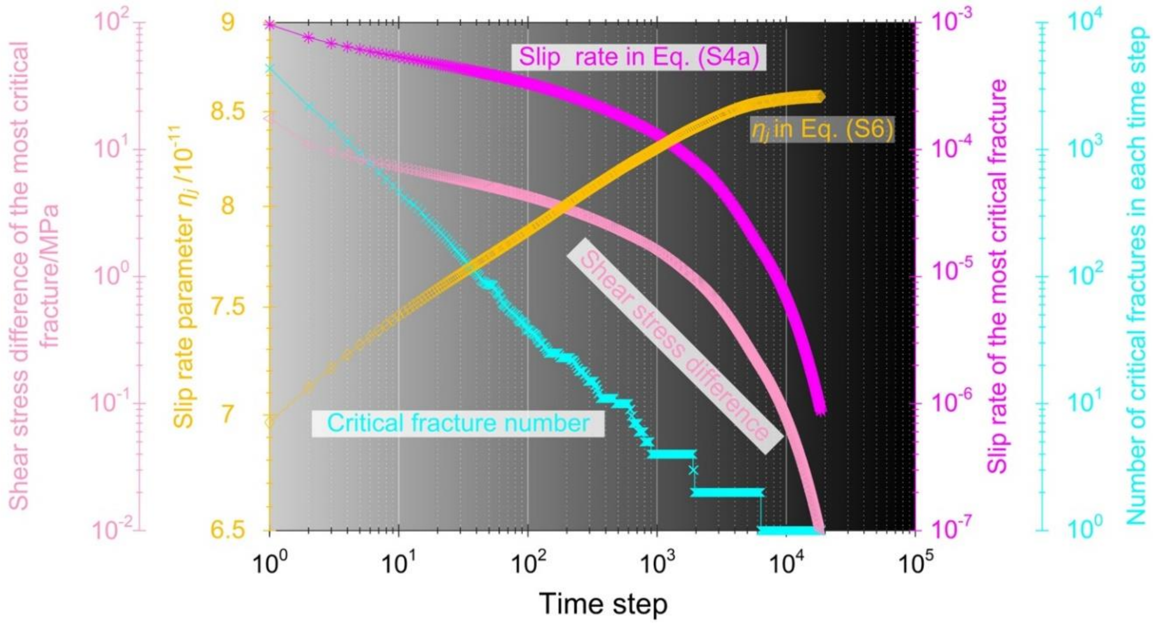

Figure S2. Evolution of slip rate parameter, slip rate, and shear stress difference of the most critical fracture, and critical fracture number in each time step in the stochastic case specified in Figure 2.

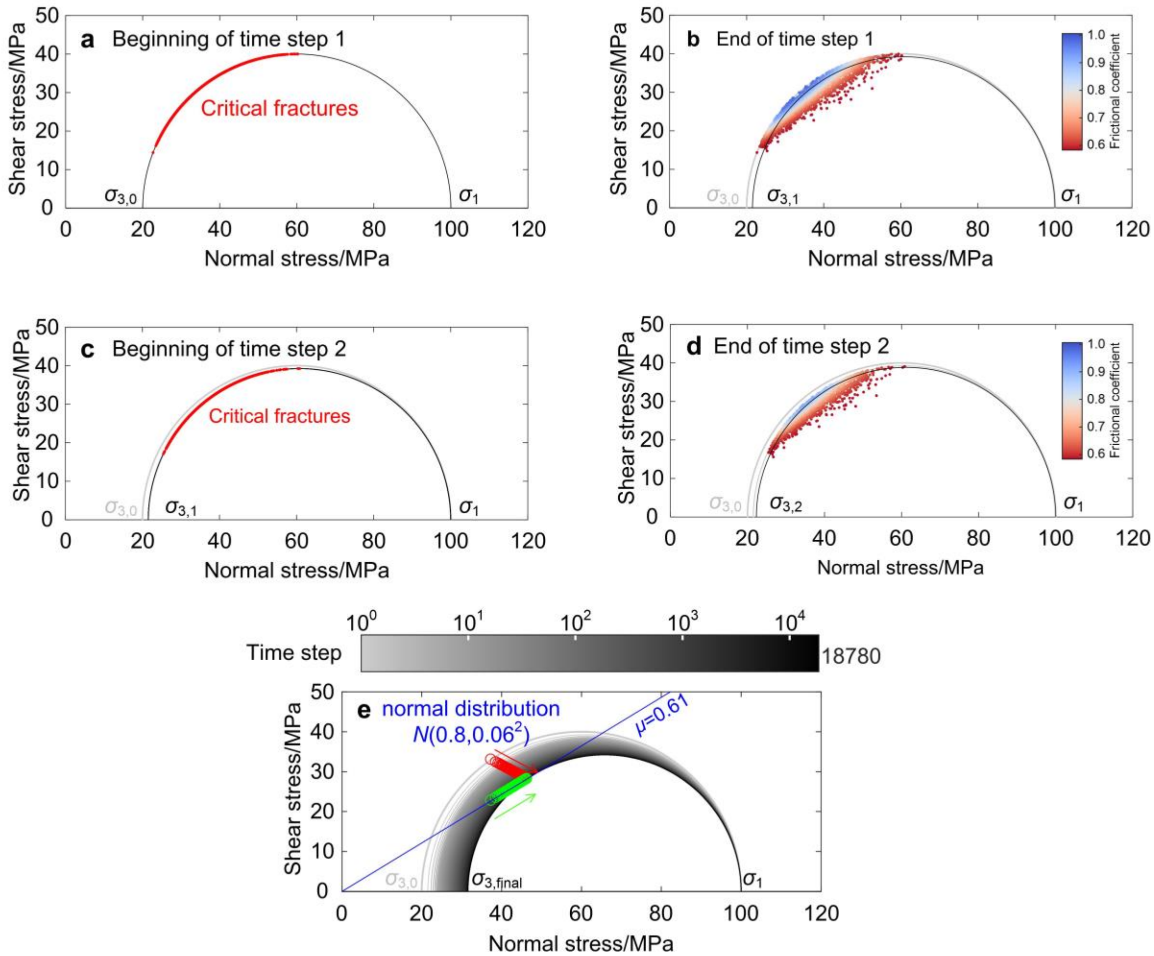

Figure S3. Stochastic case with normally distributed frictional coefficient $N(0.8, 0.06^2)$ in normal faulting stress regime: **a-d** Identification of critical fractures and stress evolution in the first two iterations. For each time step, critical fractures are identified at its beginning, which are marked as red dot on the Mohr diagram. After frictional slip, stress state of each critical fracture is colored according to its frictional coefficient. **e** Complete process of stress evolution. Red circle represents the resolved stress state surrounding the most critical fracture at each time step, while green circle is its frictional resistance. As a reference, the frictional coefficient of the most critical fracture is plotted as a solid blue line. Gray colormap is also shown with color scaled to time step. The total number of time steps is 18,780.

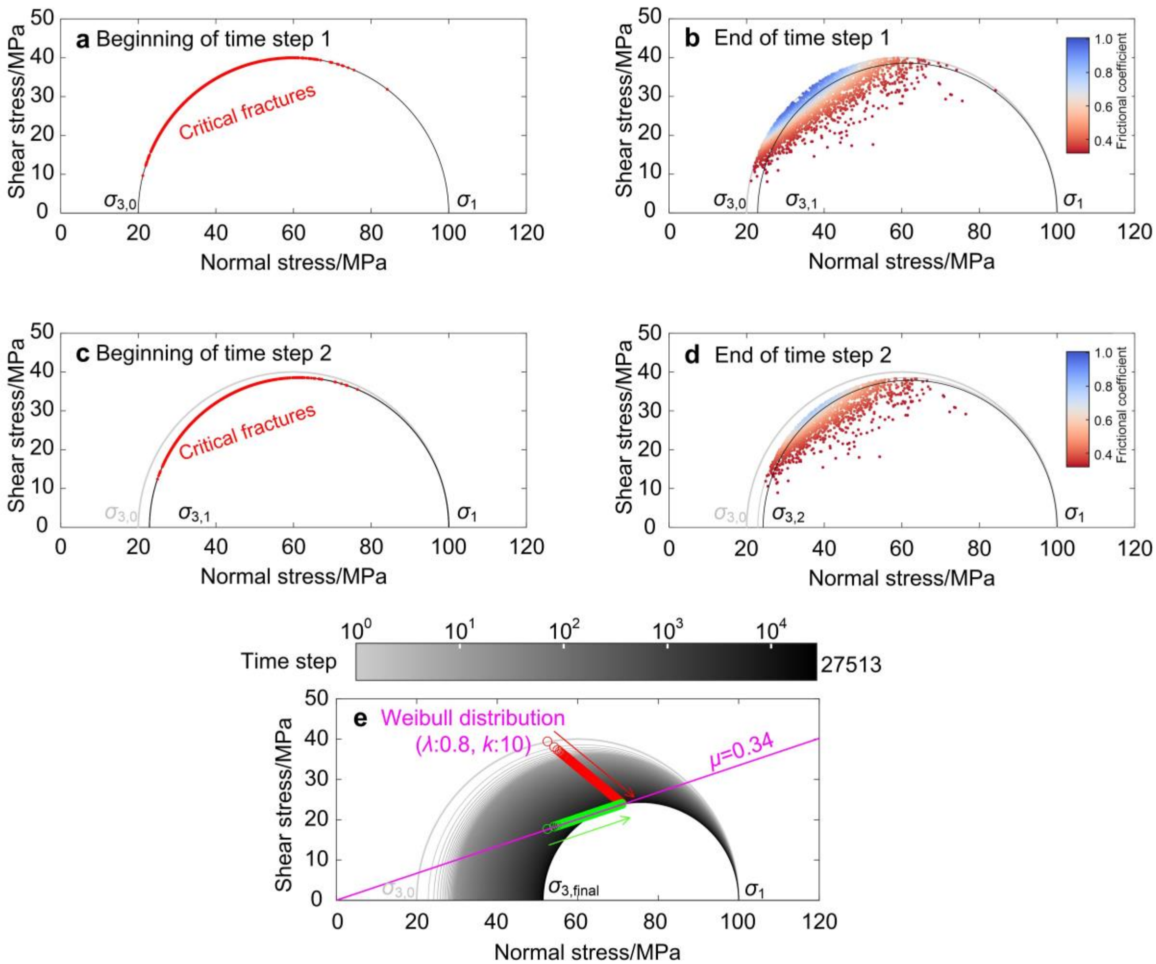

Figure S4. Stochastic system with frictional coefficient following Weibull distribution (λ = 0.8, k = 10) in normal faulting stress regime: **a-d** Identification of critical fractures and stress evolution in the first two iterations. For each time step, critical fractures are identified at its beginning, which are marked as red dot on the Mohr diagram. After frictional slip, stress state of each critical fracture is colored according to its frictional coefficient. **e** Complete process of stress evolution. Red circle represents the resolved stress state surrounding the most critical fracture at each time step, while green circle is its frictional resistance. As a reference, the frictional coefficient of the most critical fracture is plotted as a solid magenta line. Gray colormap is also shown with color scaled to time step. The total number of time steps is 27,513.

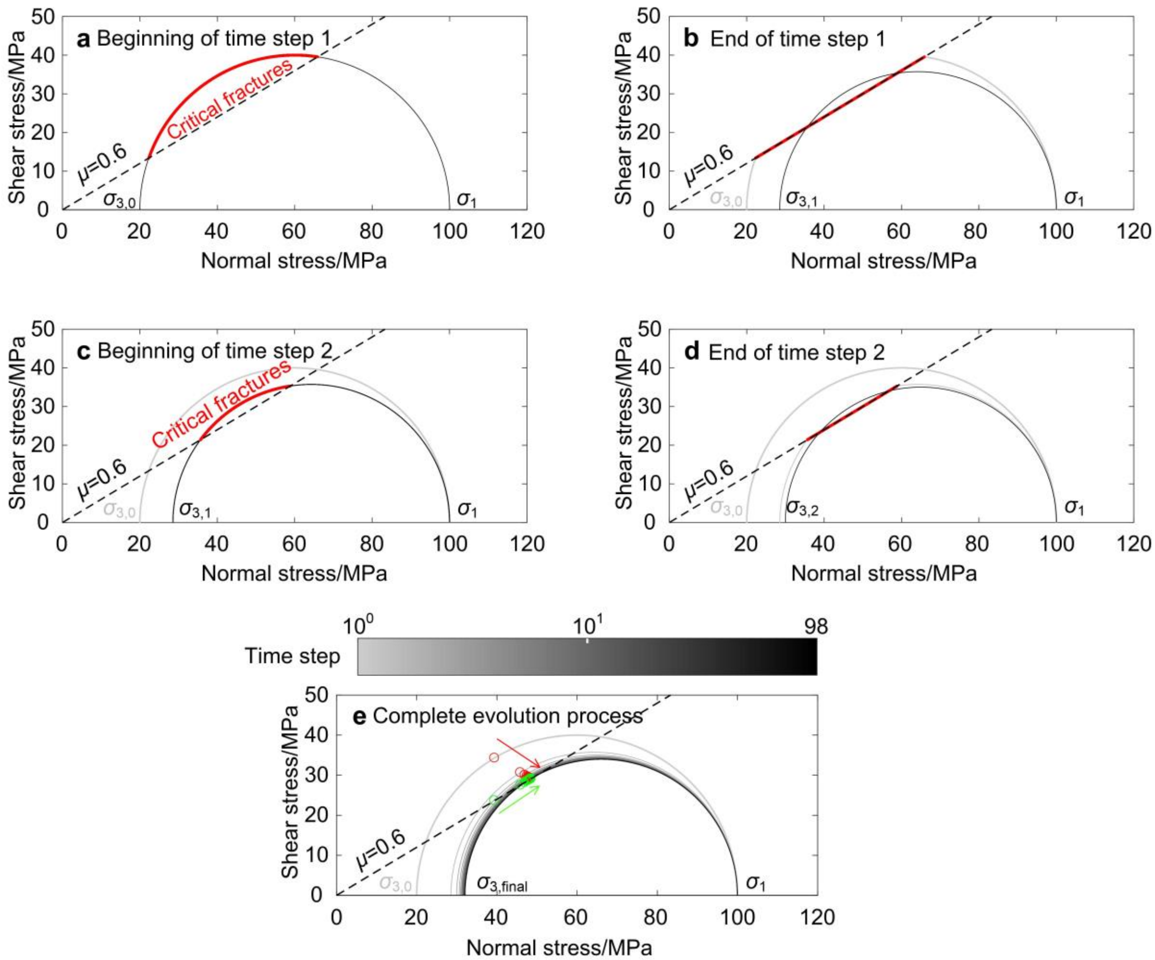

Figure S5. Deterministic case with equal frictional coefficient (0.6) in normal faulting stress regime: **a-d** Identification of critical fractures and stress evolution in the first two iterations. For each time step, critical fractures are identified at its beginning, which are marked as red dot on the Mohr diagram. After frictional slip, all critical fractures are represented as red dots on the frictional failure line (black dashed line). **e** Complete process of stress evolution. Red circle represents the resolved stress state surrounding the most critical fracture at each time step, while green circle is its frictional resistance. Gray colormap is shown with color scaled to time step. The total number of time steps is 98.

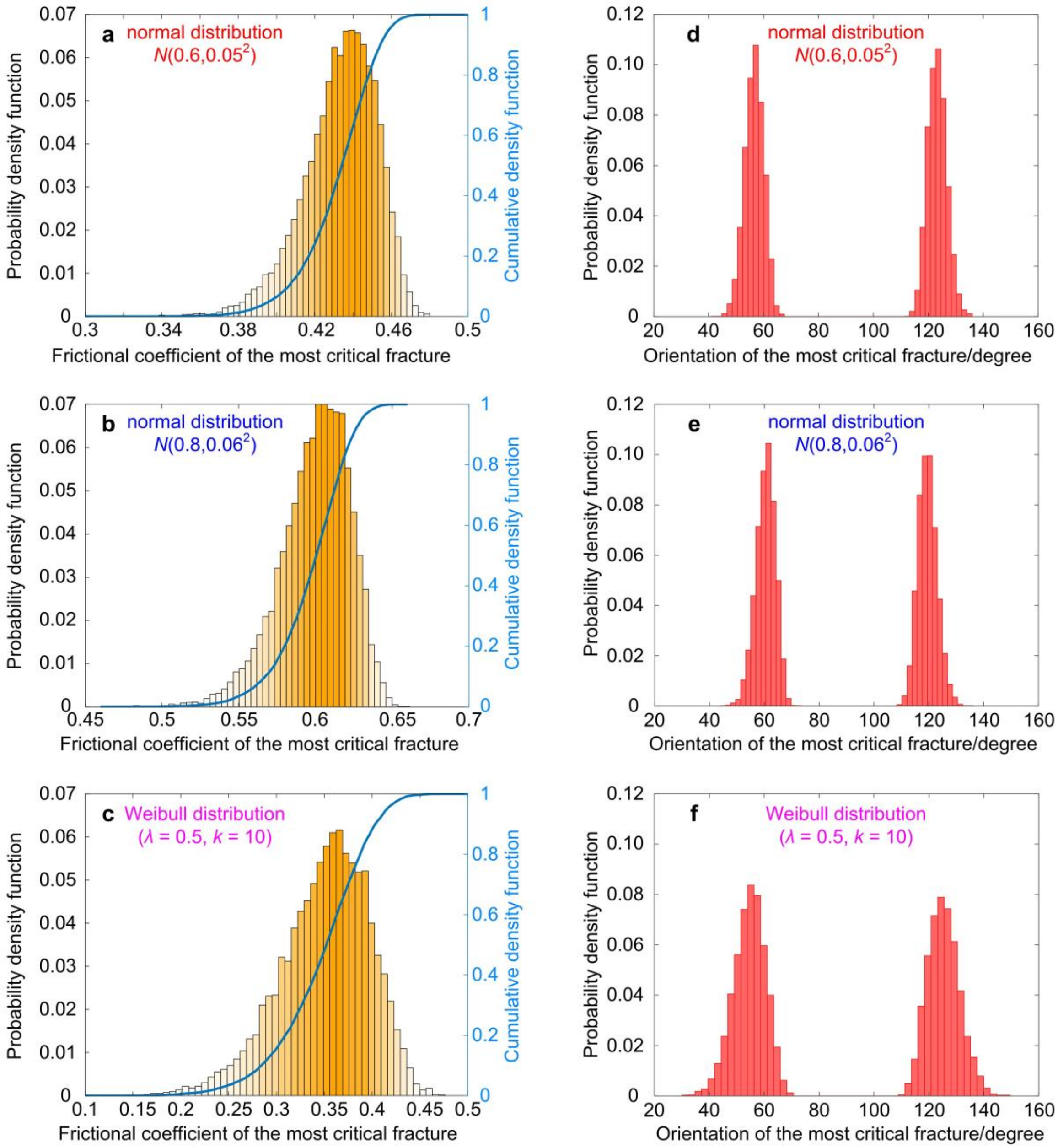

Figure S6. Probability density function of the (**a-c**) frictional coefficient and (**d-f**) orientation of the most critical fracture based on 10,000 calculations for each frictional coefficient distribution, using Monte Carlo method. The color gradient of each bin in (**a-c**) is scaled to its probability.

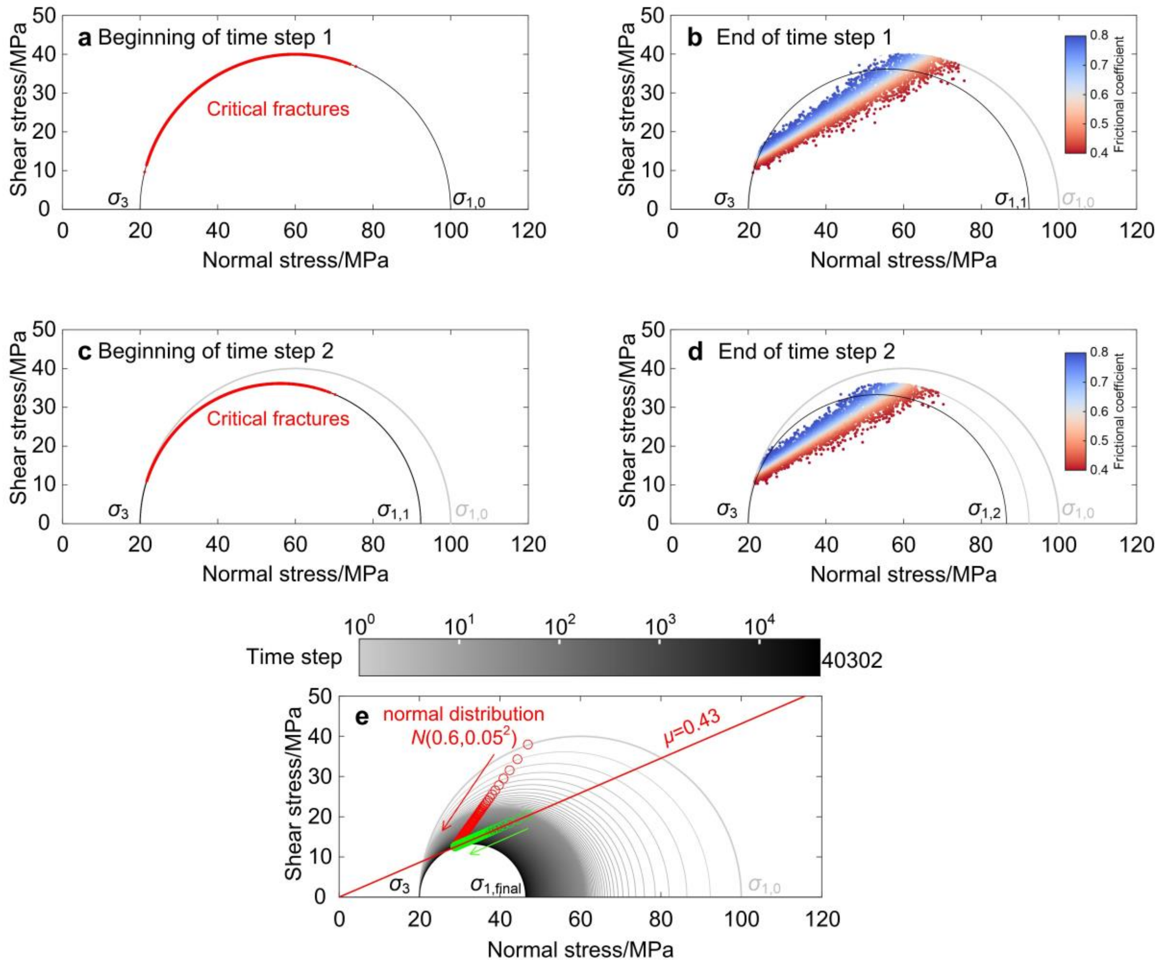

Figure S7. Stochastic system with normally distributed frictional coefficient $N(0.6,\ 0.05^2)$ in reverse faulting stress regime: **a-d** Identification of critical fractures and stress evolution in the first two iterations. For each time step, critical fractures are identified at its beginning, which are marked as red dot on the Mohr diagram. After frictional slip, stress state of each critical fracture is colored according to its frictional coefficient. **e** Complete process of stress evolution. Red circle represents the resolved stress state surrounding the most critical fracture at each time step, while green circle is its frictional resistance. As a reference, the frictional coefficient of the most critical fracture is plotted as a solid red line. Gray colormap is also shown with color scaled to time step. The total number of time steps is 40,302.

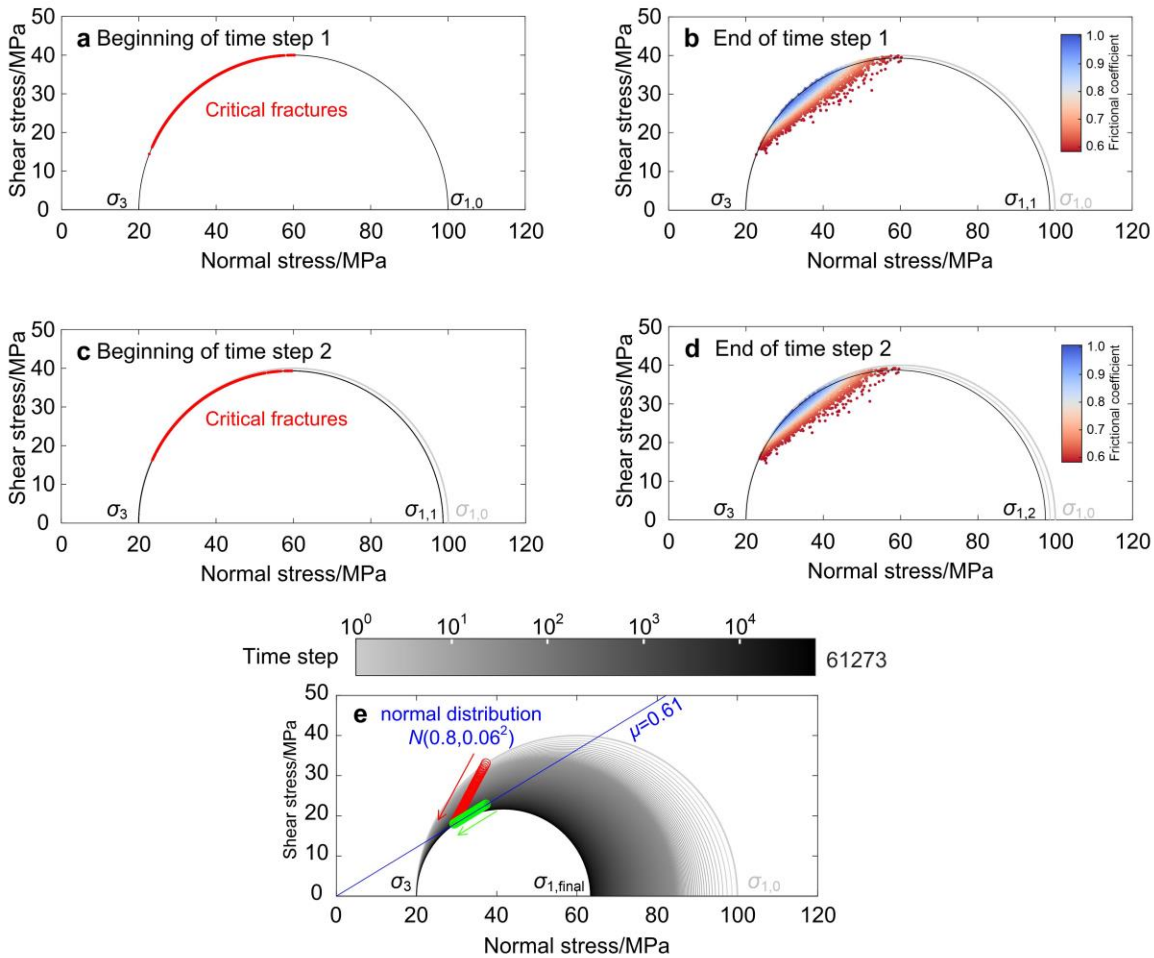

Figure S8. Stochastic system with normally distributed frictional coefficient $N(0.8,\ 0.06^2)$ in reverse faulting stress regime: **a-d** Identification of critical fractures and stress evolution in the first two iterations. For each time step, critical fractures are identified at its beginning, which are marked as red dot on the Mohr diagram. After frictional slip, stress state of each critical fracture is colored according to its frictional coefficient. **e** Complete process of stress evolution. Red circle represents the resolved stress state surrounding the most critical fracture at each time step, while green circle is its frictional resistance. As a reference, the frictional coefficient of the most critical fracture is plotted as a solid blue line. Gray colormap is also shown with color scaled to time step. The total number of time steps is 61,273.

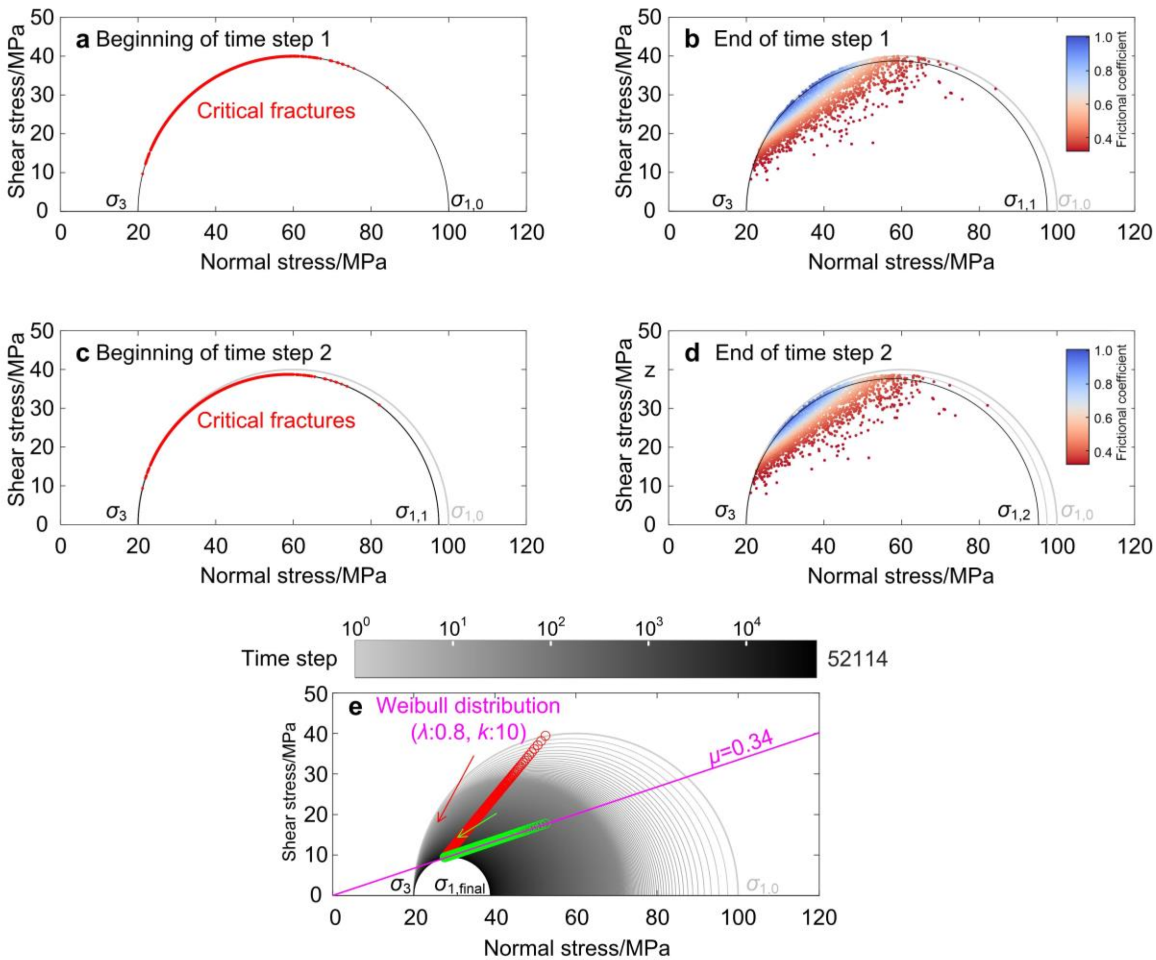

Figure S9. Stochastic system with frictional coefficient following Weibull distribution (λ = 0.8, k = 10) in reverse faulting stress regime: **a-d** Identification of critical fractures and stress evolution in the first two iterations. For each time step, critical fractures are identified at its beginning, which are marked as red dot on the Mohr diagram. After frictional slip, stress state of each critical fracture is colored according to its frictional coefficient. **e** Complete process of stress evolution. Red circle represents the resolved stress state surrounding the most critical fracture at each time step, while green circle is its frictional resistance. As a reference, the frictional coefficient of the most critical fracture is plotted as a solid red line. Gray colormap is also shown with color scaled to time step. The total number of time steps is 52,114.

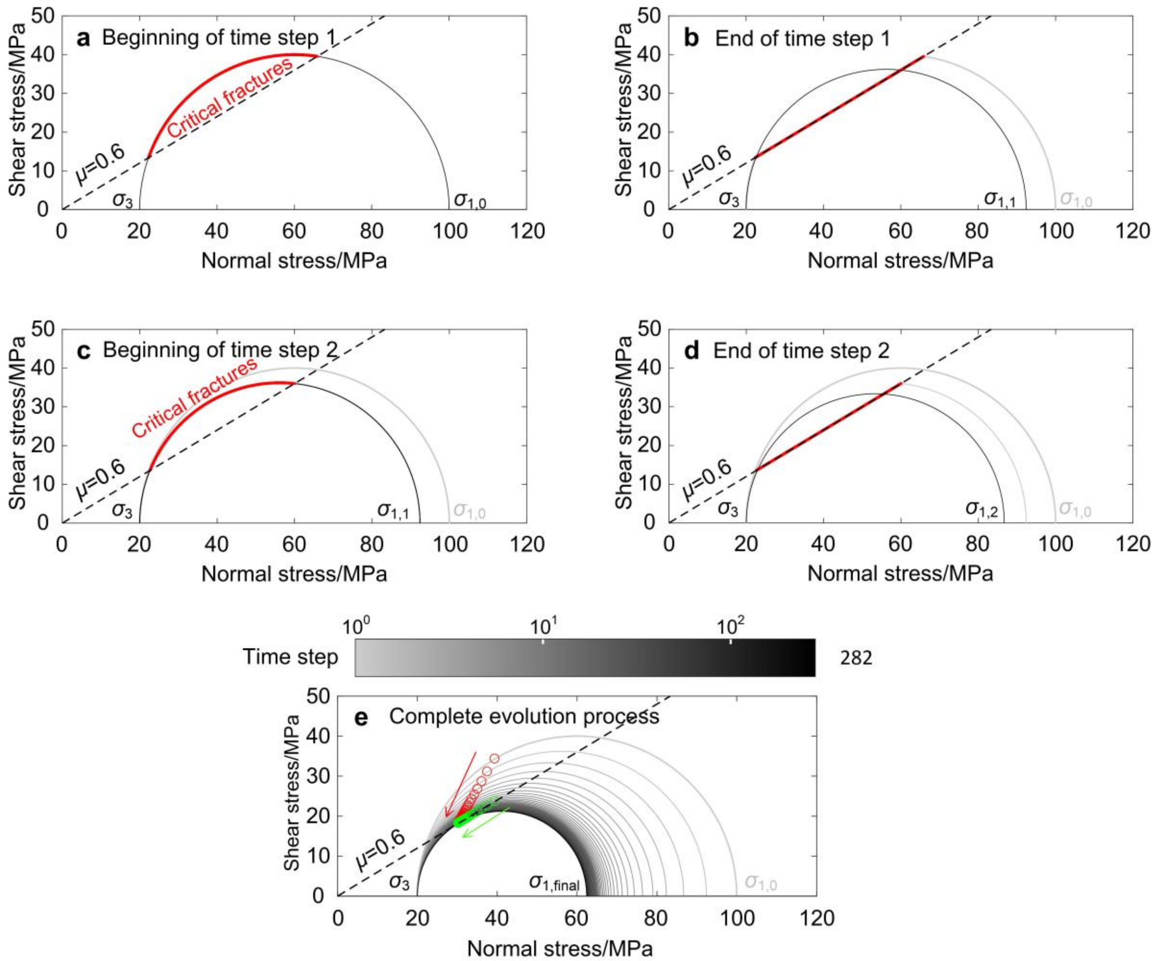

Figure S10. Deterministic case with equal frictional coefficient (0.6) in reverse faulting stress regime: **a-d** Identification of critical fractures and stress evolution in the first two iterations. For each time step, critical fractures are identified at its beginning, which are marked as red dot on the Mohr diagram. After frictional slip, all critical fractures are represented as red dots on the frictional failure line (black dashed line). **e** Complete process of stress evolution. Red circle represents the resolved stress state surrounding the most critical fracture at each time step, while green circle is its frictional resistance. Gray colormap is shown with color scaled to time step. The total number of time steps is 282.